IEEE Access
Multidisciplinary | Rapid Review | Open Access Journal

Received July 14, 2020, accepted July 24, 2020, date of publication July 28, 2020, date of current version August 7, 2020.

Digital Object Identifier 10.1109/ACCESS.2020.3012481

Comprehensive Optimization of the Unmanned Tilt-Wing Cargo Aircraft With Distributed Propulsors

GANG CHEN, DONGLI MA, YUHONG JIA, XINGLU XIA, AND CHENG HE
School of Aeronautic Science and Engineering, Beihang University, Beijing 100191, China
Corresponding author: Gang Chen (mrchey@buaa.edu.cn)

ABSTRACT The unmanned tilt-wing cargo aircraft using distributed propulsors is an emerging aircraft significantly different from traditional types. This paper proposes an aerodynamic, propulsion, noise, weight integrated optimization design method for this new aircraft. The method consists of several functional modules specially developed or adjusted targeting the aircraft's characteristics, such as the boundary state analysis, propeller/rotor oblique inflow analysis, waked wing analysis, propeller/rotor noise evaluation, multi-state wing mass analysis, multi-objective genetic algorithm optimization. It comprehensively considers the impact of various complex factors on the optimization results, such as the impact of distributed propulsors on the wing aerodynamics, the effect of wingtip propellers on the induced drag reduction, the coupling between wing aerodynamics and structure, the propeller/rotor aerodynamics optimization, and noise control. With the proposed method, it is possible to directly translate the top-level design requirements into the design scheme with the optimal specific system performance (such as the lowest delivery cost and highest delivery efficiency) at the very initial aircraft design stage, thereby greatly shortening the development cycle. A case study was presented. The results show that the introduction of distributed propulsors can increase the delivery efficiency by 28.2% and reduce the delivery cost by 15%; suppressing the wingtip vortices using propellers can increase the wing lift-drag ratio by 5.43%-6.65%; the slipstream generation efficiency and thrust efficiency are significantly different between different distributed propulsor schemes. To maximize the overall efficiency, it is necessary to balance between the slipstream generation efficiency and the overall thrust efficiency when optimizing the tilt-wing cargo aircraft.

INDEX TERMS Convertiplane, cargo aircraft, unmanned aerial vehicle, vertical takeoff and landing, aircraft multidisciplinary optimization.

I. INTRODUCTION

With the explosive growth of global e-commerce in recent years, consumers' demand for air cargo has increased significantly, and continues to increase at a rate of 4.4% per year [1]. According to Boeing's forecast, in the next 20 years, the freight volume will triple, and the freight fleet will grow by 75% [2]. Among these fleet, the unmanned cargo aircraft plays an important role. Compared with conventional logistics methods, the unmanned cargo aircraft gets rid of the dependence on road infrastructure, and is very suitable for using between islands [3] or in some developing countries without complete road network, and also in the remote area of developed countries [4]. By establishing the point-to-point freight route between the cargo warehouse and the distribution center, or between the central airport to the small airports, [5] the unmanned cargo aircraft provides the possibility of greatly improving freight efficiency and reducing costs. In the meantime, it provides a fast and reliable solution for emergency transportation in complex scenarios such as the earthquake or other disasters. At present, there are many companies that have carried out and implemented the unmanned cargo aircraft project, such as Google, Amazon, UPS, DHL, etc.

The unmanned cargo aircraft can be generally divided into three types – multirotor aircraft, fixed-wing aircraft, and converting aircraft such as tilt-wing aircraft [6]. Among them, the unmanned tilt-wing cargo aircraft combines the advantages

The associate editor coordinating the review of this manuscript and approving it for publication was Moayad Aloqaily.

of the multirotor and fixed-wing aircraft, which can not only take off and land vertically, but also has a fast cruise speed and high cruising efficiency. The combination of flexibility and efficiency makes this freighter have outstanding development potential in future cargo scenarios.

In recent years, a large number of studies on convertiplane have been conducted, which mainly focus on the determination of overall parameters (such as the total takeoff weight, wing loading and aera, design power, or mass distribution), propeller/wing interference, dynamic modeling methods, and control strategies. These studies have gone through several stages of development. Early methods for determining the overall parameters were mainly based on statistical data [7]. These methods neglect specific aircraft types, takeoff mass, and mission categories, which may lead to design results with high power redundancy. To improve the credibility of the design results, the researchers introduced momentum theory into the parameter determination process to recalculate the power load [8]–[10]. The aircraft design space has also expanded from the composite design space of fixed-wing mode and rotor mode to a comprehensive design space integrating transition mode and traditional constraints [11]. With the gradual improvement of the design method, the complexity and confidence of the propeller/rotor aerodynamic description continue to increase, which changes from the earliest experimental-based empirical method [7] to momentum theory, [12] Blade Element Method (BEM), [13] Blade Element Momentum Theory (BEMT), [14] Vortex Lattice Method (VLM), [15] Computational Fluid Dynamics (CFD) method, [16] etc. The description about the most important aerodynamic phenomenon - the propeller/wing interference, has also gone through the development from the simple momentum theory, [17] the combination of BEMT and VLM, [18] to the CFD method based on actuator disk [19] or dynamic grid [20]. On the basis of the above tools, researchers have carried out a lot of work about the dynamics modeling of the tilt-wing aircraft, and established the simplified model-based tilt-wing aircraft dynamics equations [21] and the equations based on tensor flight dynamics technology, [22] which laid the foundation for the controller design of this type of UAV [23]–[25] and the operating strategy optimization in each flight mode [26]. Meanwhile, there are also many valuable research works focusing on the drag reduction of tilt-wing aircraft, [27] rotor aerodynamic/noise optimization, [28]–[30] structural design, [31] analysis about flutter [32] or ground effects [33].

In addition to the above research, the application of advanced technology concepts such as the distributed electric propulsion (DEP) in the field of tilt-wing aircraft is also deepening. DEP is a basic technology proposed by NASA in recent years for the concept of transitional mobility (such as ODM) [34], which was first used in the field of fixed-wing aircraft. This technology uses a series of propellers installed along the wing leading edge to accelerate the airflow, thereby effectively improving the low-speed lift characteristics, reducing the wing area, and thus improving cruise efficiency [35]. At present, although the DEP technology has been used in tilt-wing aircraft such as GL-10 [36] and Vahana [37], its application mechanism and effect are not yet clear. In principle, the DEP equipped on tilt-wing aircraft is very different from that on fixed-wing aircraft. The DEP for fixed-wing aircraft only focuses on the slipstream generation, whereas the scheme for tilt-wing aircraft should not only consider the slipstream, but also pay full attention to the thrust efficiency during vertical takeoff and landing. This requirement difference leads to the difference in the design methods and application benefit of DEP schemes in the two types of aircraft.

From the perspective of development trends, the unmanned tilt-wing cargo aircraft are constantly moving towards high efficiency, low noise, and low power consumption. The development cycle tends to be shortened, and the requirements for designers are also constantly increasing. Therefore, disciplines such as propeller/rotor aerodynamic optimization, propeller/wing interference, noise assessment, weight assessment, advanced propulsion system application, and basic aircraft platform design should not be used as discrete design modules, instead, they should be formed as a unified optimized design process. In this way, the overall parameters, aerodynamic shape, propeller/rotor aerodynamics and noise, propeller wing interference, aerodynamic structure coupling, and other issues can be fully considered at the initial aircraft design stage, thereby effectively reducing the number of design iterations.

The multi-disciplinary optimization method has continued to attract researchers' attention in recent years, and is increasingly used in the design process of various new types of aircraft (such as the fly wing [38], unmanned helicopter [39], solar plane [40], and morphing wing aircraft [41], [42]) or their components or subsystems [43], [44]. However, there is little research on the multidisciplinary optimization for the unmanned DEP tilt-wing cargo aircraft.

To compensate for the shortcomings of existing research, this paper proposes a comprehensive optimization design method for unmanned tilt-wing cargo aircraft with distributed propulsors. The method comprehensively considers the propeller/rotor optimization, noise evaluation, propeller/wing interference, and aerodynamic/structure coupling, which can output the design results with the optimal specific system performance (such as lowest delivery cost and highest delivery efficiency), including the optimal propeller/rotor number and geometric parameters, wing geometry, power system design, cruise speed, etc. Several functional modules are included in this method, such as the boundary state analysis, oblique inflow BEMT analysis, waked wing analysis, propeller/rotor noise evaluation, multi-state wing mass analysis, etc. These modules together form an integrated aerodynamics, noise, structure, powertrain optimization process based on the multi-objective genetic algorithm. The detailed implementation process of this method is described in Sections 2 and 3. In Section 4, the method is applied for the optimization of a 200-kg unmanned tilt-wing cargo aircraft in

a 100-km cargo scenario, which proves the validation of this method.

II. MATHEMATICAL-PHYSICAL MODELS

A. BOUNDARY STATE ANALYSIS

The flight modes of the tilt-wing cargo aircraft performing typical mission mainly include three types, namely, rotor mode, conversion mode, and fixed-wing mode (see Fig. 1). Among them, the rotor mode refers to the flight state where the wing tilt angle θ_t (angle of the wing chord relative to its initial position) equals to 90° and all the propellers and rotors operate; the fixed-wing mode refers to the flight state with θ_t equal to 0°, where all rotors are folded back, and only propellers operate; the flight status between the rotor mode and fixed-wing mode is the transition mode.

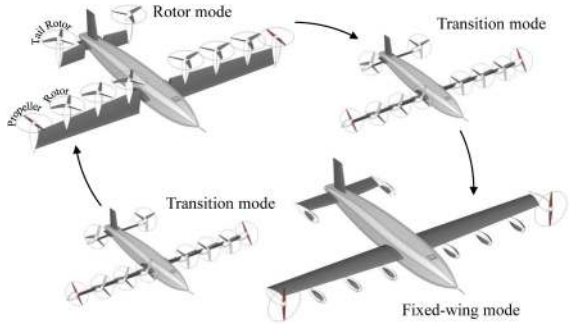

FIGURE 1. Configuration and flight modes.

In the initial mission stage, the aircraft converts from the rotor mode to the fixed-wing mode through a specific conversion trajectory (see path 1, path 2 in Fig. 2), and returns to the rotor mode when the mission ends. The conversion trajectory can be set in advance or adjusted in real-time by the flight controller according to the flight status such as velocity, altitude, and pitch angle rate [26]. In both ways, the trajectory should lay in the conversion corridor defined by the high-speed conversion boundary (right boundary) and the low-speed conversion boundary (left boundary) [45], [46]. The wider the conversion corridor, the greater the adjustment margin of the conversion trajectory, and thus the safer the conversion process [45]. The corridor width can be adjusted by controlling the position of the five boundary status points in the Fig.2. These points belong to different flight modes, as listed in Table 1.

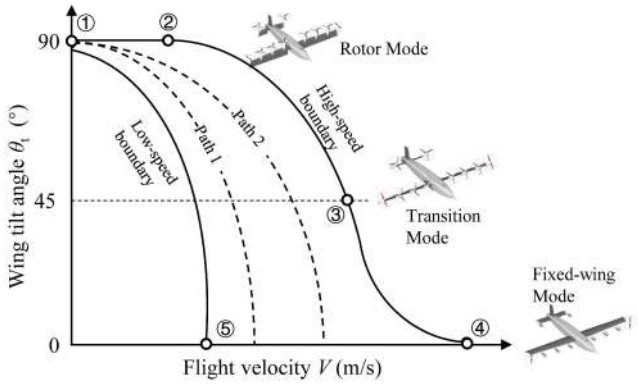

FIGURE 2. Transition corridor and boundary status points.

TABLE 1. Boundary status points.

Status	Number	Flight mode	Tilt angle	Velocity
Hover	1	Rotor mode	90°	0
Maximum-speed forward flight	2	Rotor mode	90°	V_1
Cessation-speed flight	3	Transition mode	45°	V_c
Maximum-speed flight	4	Fixed-wing mode	0°	V_{max}
Minimum-speed flight	5	Fixed-wing mode	0°	V_{min}

Among the five boundary states, the position of states 1-4 constitutes the main constraints on the maximum output power of the aircraft, while the position of states 5 places requirements on the maximum lift coefficient of the aircraft when the distributed propulsors operate. Both aspects affect the design of the wing, tail, propellers, and rotors.

Fig. 3 shows the static force analysis of the tilt-wing aircraft in each boundary state, where T_1 represents the thrust of the wing-mounted propeller/rotor, and T_2 the tail-mounted. N_1 and N_2 are the corresponding propeller/rotor normal force; L, D, G, and $M_{y,a}$ represent the whole aircraft lift, drag, gravity, and aerodynamic pitching moment considering the propeller slip flow effect, respectively; α and θ represent the angle of attack, the pitch angle of the fuselage; V_0 the far-field velocity. Therefore, the resultant forces and moment of the aircraft in the XZ plane of the fuselage coordinate system can be uniformly expressed as:

$$F_X = \sum_{i=1}^{2} (T_i \cos\theta_1 - N_i \sin\theta_1) + L\sin\theta_2 - D\cos\theta_2 - G\sin\theta \quad (1)$$

$$F_Z = \sum_{i=1}^{2} (T_i \sin\theta_1 + N_i \cos\theta_1) + L\cos\theta_2 + D\sin\theta_2 - G\cos\theta \quad (2)$$

$$M_Y = \sum_{i=1}^{2} \left(T_i l_i \sin\theta_t + N_i \left(l_i \cos\theta_t + l_i'\right)\right) + M_{y,a} \quad (3)$$

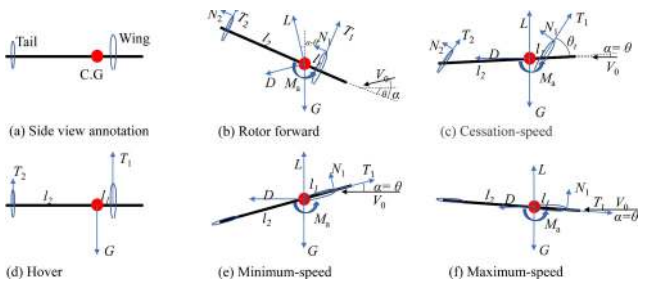

FIGURE 3. Static force analysis of boundary status points.

where $\theta_1 = \theta_t + \theta$, $\theta_2 = \alpha - \theta$, l_i are the distance between wing/tail rotation axis and aircraft gravity, and l_i' between wing/tail rotation axis and propeller/rotor disk. To ensure flight safety, regardless of the values of the wing, propeller, and rotor parameters, $F_x \geq 0, F_z \geq 0, M_y = 0$ should be kept under each boundary condition.

B. PROPELLER/ROTOR AERODYNAMICS

Propeller/Rotor aerodynamics and slip flow distribution is calculated based on the propeller/rotor aerodynamic model. There are many methods developed for the propeller/rotor aerodynamic calculation, such as the momentum method [12], BEM [13], BEMT [14], VLM [15], CFD method [16], etc. Among them, the BEMT not only considers the detailed propeller/rotor geometry and airfoil aerodynamics, but also describes the slip flow characteristics with high fidelity. All these functions can be achieved with a small amount of calculation, which makes the BEM method one of the most suitable propeller calculation methods for system-level optimization.

1) AIRFOIL PRECALCULATION

The predicted accuracy of the BEMT method highly depends on the accuracy of airfoil aerodynamic input. In this research, the airfoil aerodynamic database (Re=5 × 10^4-3 × 10^6, α = 10°-18°) was firstly generated by the CFD solver, and then extended to a larger α range using the AERODAS model [47]. Meanwhile, the impact of the finite blade span on the airfoil aerodynamics was considered using the method proposed by Jacobs and Anderson [48], and the stall delay effect of the rotating blade was corrected using the method proposed by Elgammi [49].

2) OBLIQUE INFLOW BEMT METHOD

The classic BEMT method adopts the axial inflow assumption, which can be applied for the propeller/rotor calculation in states 1 and 4 (see Table 1), but is less suitable for states 2, 3, and 5 since the oblique inflow angles of propeller/rotor in these states cannot be neglected. In these oblique inflow states, the angle of attack and inflow speed of each blade element change periodically as the blade rotates. Therefore, it is necessary to correct the axial inflow assumption and form an oblique inflow BEMT method. At any radius station r, the thrust, normal force, and torque of the blade element are no longer represented using the single value of fixed rotation phase, but using the time-average value of the entire rotation period, as shown in the following equations: [50]

$$\overline{T}(r) = \frac{N_b}{2\pi}\int_0^{2\pi}(L_e(r,\psi)\cos\beta - D_e(r,\psi)\sin\beta)\,d\psi \quad (4)$$

$$\overline{F_t}(r) = \frac{N_b}{2\pi}\int_0^{2\pi}(L_e(r,\psi)\sin\beta + D_e(r,\psi)\cos\beta)\,d\psi \quad (5)$$

$$\overline{Q}(r) = \frac{N_b}{2\pi}\int_0^{2\pi}(L_e(r,\psi)\sin\beta + D_e(r,\psi)\cos\beta)\,rd\psi \quad (6)$$

where N_b is the total blade number, ψ the blade phase angle, β the induced angle. L_e and D_e represent the blade element lift and drag under local velocity and angle of attack. Another expression of the propeller aerodynamics at radius r based on the Glauert's momentum theory has the following form:

$$\overline{T}(r) = 4\rho\pi r\bar{u}_0(r)\left[V_a^2 + 2V_a\bar{u}_0(r)\cos\delta + \bar{u}_0(r)^2\right]^{0.5}dr \quad (7)$$

$$\bar{Q}(r) = 4\rho\pi r^2\bar{V}_{t0}(r)[V_a^2 + 2V_a\bar{u}_0(r)\cos\delta + \bar{u}_0(r)^2]^{0.5}dr \quad (8)$$

where δ represents oblique inflow angle, $\bar{u}_0$ the time-averaged axial induced speed, and V_{t0} the time-averaged circumferential induced speed. Based on (4)-(8), the values of $\bar{u}_0$ and V_{t0} can be solved using Newton iteration method [51]. The time-average thrust, normal force, and torque of the blade element can be solved consequently. Integrating these forces and torque along the radius yields the overall propeller aerodynamics under the inclined inflow condition.

3) PROPELLER PERFORMANCE COMPARISON

To verify the effectiveness of the combination of the above airfoil precalculation method and the oblique inflow BEMT method, the predicted results are compared with the experimental data provided by Mc Lemore *et al.* [52] The tested propeller is a 4-blade propeller with NACA 16-Series airfoil and a diameter of 5.33 feet. The variation of the thrust coefficient C_t and power coefficient C_p with advanced ratio under oblique inflow conditions is shown in Fig.4 for several sets of installation angles. The error between the test result and the predicted result is negligible in the linear segment. Although the error increases with the deviation of the operating state, the maximum error value is still less than 8%.

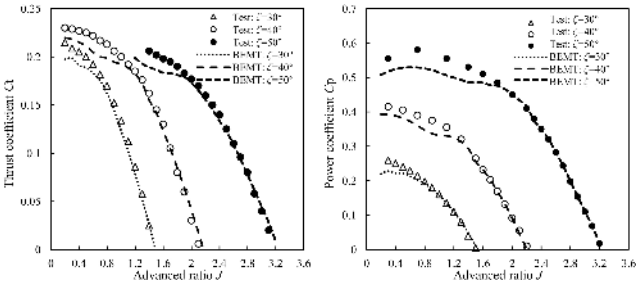

FIGURE 4. Comparison of propeller test results and predicted results under 15° oblique inflow condition where ζ represents the propeller installation angle.

C. WAKED WING MODELING

For the tilt-wing aircraft with a distributed propeller/rotor arrangement, the interference of the propeller/rotor wake on the wing is reflected in two aspects: one is the drag reduction caused by the wingtip propeller in fixed-wing cruise state; the second is the lift increase induced by the propeller/rotor in transition mode (states 3) and fixed-wing minimum speed state (state 5). These two interference phenomena have a great influence on the aircraft design parameters (such as design power and wing area), making it necessary to analyze their effects at the initial design stage. There are several methods

for the waked wing analysis, such as the simplified momentum method [17], VLM method [18], CFD method based on actuator disk [19] or dynamic grid [20]. Among them, the VLM method can describe the detailed distribution of propeller/rotor slip flow, and has a relatively fast calculation speed, making it suitable for the system-level optimization process. Since the tilt-wing aircraft will encounter the high angle of attack during states 3 and 5, the nonlinear aerodynamic characteristics are required to be captured. To this end, the nonlinear VLM method is adopted in this research.

1) ADAPTIVE GRID GENERATION

To capture the detailed distribution of the propeller/rotor slipstream and speed up the calculation speed, an adaptive grid generation approach is used for the nonlinear VLM method. The grid number and distribution are adjusted according to the propeller/rotor number and operating state, as shown in Fig. 5. For a given wing shape, a sparse reference grid will be generated at first. Then, an encryption area with a grid number of not less than 10 is generated in each propeller/rotor wake area. The transition between the encryption area and the sparse area is conducted using interpolation.

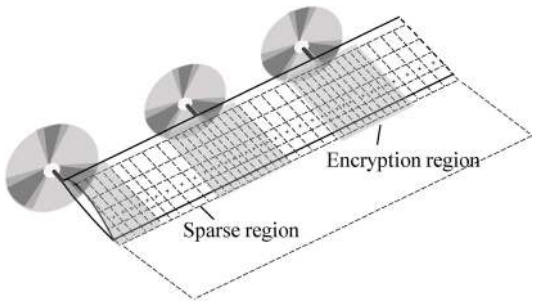

FIGURE 5. Adaptive grid generation.

2) NONLINEAR VLM METHOD

The vortex line arrangement of the nonlinear VLM is basically the same as the linear VLM method. The main difference is that the nonlinear VLM adds an additional set of viscous control points for the effective angle of attack determination at the 3/4 position of each string chord (see the dots in Fig. 5). By introducing the perturbation circulation $\Delta\boldsymbol{\Gamma}$ to the linear VLM circulation solution $\boldsymbol{\Gamma}$ on each vortex lattice, the effective inflow angle of attack and pressure distribution can be corrected, making the pressure distribution of each string chord approximately equal to the two-dimensional viscous result [53]. The specific implementation steps of this method are as follows:

1) Use the CFD solver to generate the distribution of pressure difference between the upper and lower airfoil surfaces under different Reynolds numbers and different angles of attack, and establish an interpolation database;

2) Set the non-penetrating conditions at each control point with local inflow velocity (with or without propeller/rotor slipstream), and use linear VLM method to solve the circulant matrix $\boldsymbol{\Gamma}$;

3) Add an additional circulation $\Delta\boldsymbol{\Gamma}$ at each vortex lattice, calculate the pressure coefficient of each panel with $\boldsymbol{\Gamma}+\Delta\boldsymbol{\Gamma}$, and output the effective angle of attack calculated at the viscous control point of each strip;

4) Use the effective angle of attach and viscous pressure interpolation database to obtain the viscous pressure distribution of each panel, establish the $\boldsymbol{J}$ matrix based on the linear pressure distribution (equal to $\boldsymbol{F}_i\boldsymbol{n}_i/A_i$, where $\boldsymbol{F}_i$, $\boldsymbol{n}_i$, and A_i represent the panel force, normal direction, area, respectively) and viscous pressure distribution $\Delta C_{\mathrm{p},i}^{\mathrm{visc}}$ as in (9), solve $\boldsymbol{\Delta\Gamma}$ with Newton iteration method, then output the final nonlinear pressure distribution.

$$\boldsymbol{J}=\begin{bmatrix}\frac{\partial(-\boldsymbol{F}_i\cdot\boldsymbol{n}_i)}{\partial\Delta\boldsymbol{\Gamma}_k}+\boldsymbol{A}_i q_\infty\frac{\partial\left(\Delta C_{p,i}^{\mathrm{visc}}\right)}{\partial\Delta\boldsymbol{\Gamma}_k} & 0\\ \boldsymbol{v}_{ik}\cdot\boldsymbol{n}_i & \boldsymbol{I}\end{bmatrix} \tag{9}$$

The method can be used to calculate the nonlinear lift and induced drag distribution under the impact of propeller/rotor wake and viscous separation. The total drag of the wing is equal to the sum of the induced drag and the integration of the 2-D profile drag along the wingspan:

$$C_{\mathrm{D}}=C_{\mathrm{Di}}+\frac{1}{S}\int_{-b/2}^{b/2}C_{\mathrm{d0}}(y)\,c(y)\,\mathrm{d}y \tag{10}$$

where b is the wingspan, C_{Di} is the induced drag coefficient calculated by nonlinear VLM method. c and C_{d0} represent the local airfoil chord length and profile drag, respectively.

3) NONLINEAR AERODYNAMIC AND PROPELLER ON WING VALIDATION

We extracted three examples from existing studies to validate the proposed method. The first example was taken from NACA Technical Note 1208 [54]. The wing adopts a medium aspect ratio and NACA 6-series airfoil. The test results of the lift coefficient in the angle of attack range from $-3\,^\circ$ to $24\,^\circ$ are shown in Fig. 6a along with the corresponding predicted values. Compared with the linear VLM, the predicted accuracy of the nonlinear VLM is significantly improved in the high α region. The second test data is taken from the ProWim model provided by Veldhuis *et al.* [55]. The ProWim model consists of a straight wing with NACA 64_2A015 and a four-blade NACA5868-9 propeller [56]. Fig.6b shows the test results and predicted results in propeller-off, propeller-inboard-up, propeller-outboard-up states, which shows satisfactory consistency. The last test data comes from [57], in which a 9.33-inch four-blade propeller was installed at the tip of the wing with NACA 64_2A615 and a span of 0.73 m. The overall lift and drag polar including the propeller force were measured at the wind tunnel tests at different propeller advanced ratios, as seen in Fig. 6c. The corresponding results predicted by the nonlinear VLM and oblique-inflow BEMT are also presented, which show good agreement with the test data, especially in the low and medium C_{L} ranges.

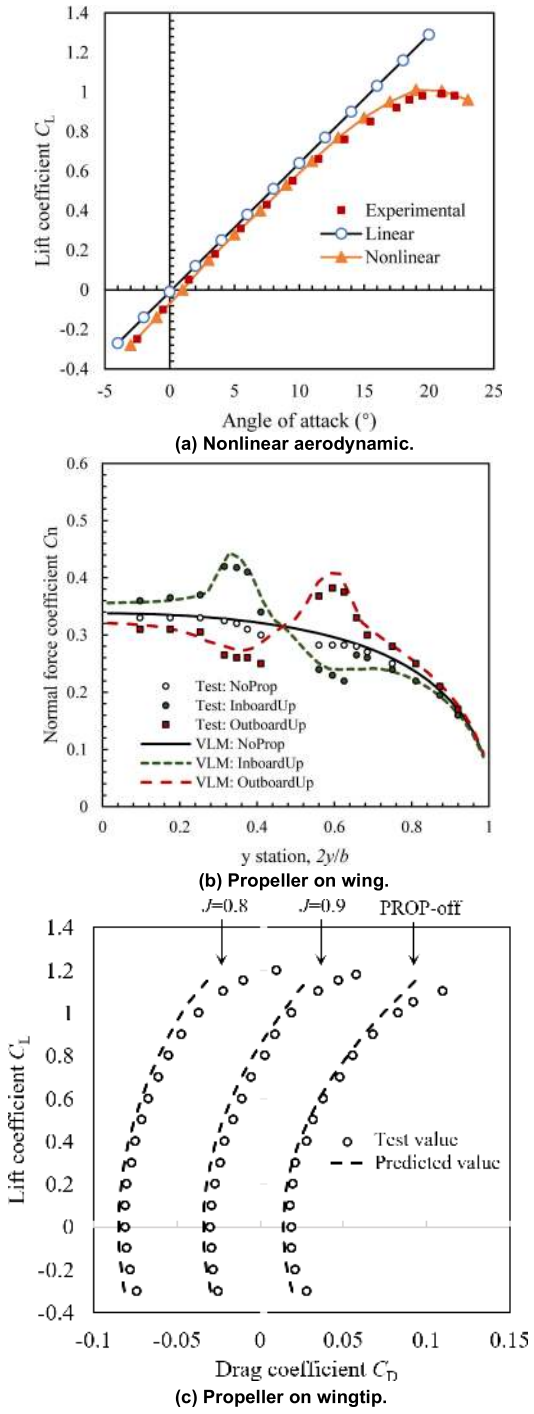

(a) Nonlinear aerodynamic.

(b) Propeller on wing.

(c) Propeller on wingtip.

FIGURE 6. Nonlinear VLM method validation.

D. PROPELLER/ROTOR NOISE

Noise control is an important issue that should be considered at the initial aircraft design stage. The propeller/rotor noise counts for the major part of the overall noise of the tilt-wing aircraft, especially when the aircraft is in the hovering state which is close to the ground and with high operating power. Represent the altitude of the noise monitoring hovering state as h. The total four noise monitoring points are set on the circle centered on the horizontal ground projection of the aircraft gravity center and taking r as the radius, as shown in Fig. 7a. The average value of the noise monitored at the four points is taken as the final noise value of the aircraft.

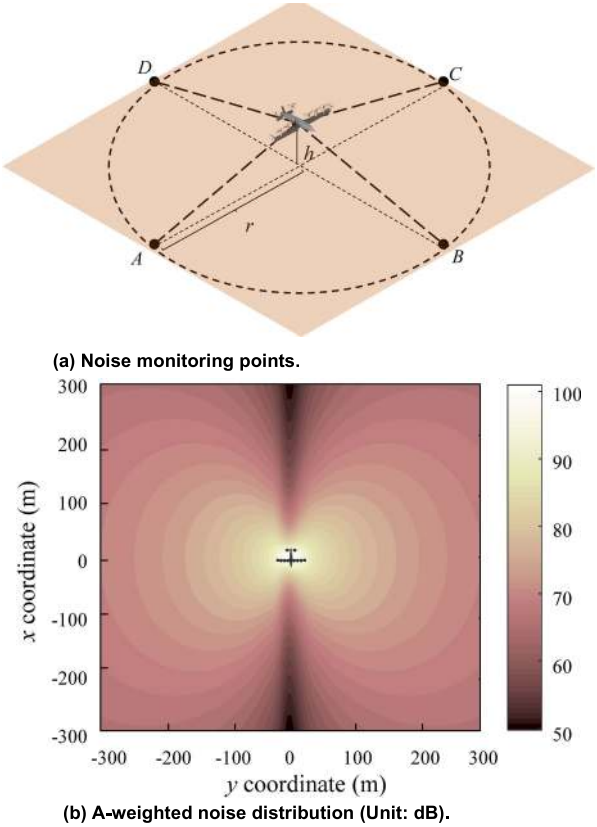

(a) Noise monitoring points.

(b) A-weighted noise distribution (Unit: dB).

FIGURE 7. Propeller/Rotor noise monitoring.

With known propeller/rotor installation position, geometry, and operating conditions, the noise at each monitoring point can be calculated by using the propeller noise code developed by Tingey and Ning [58] based on the acoustic modeling method proposed by Brooks, Pope, and Marcolini (i.e., the BPM equation) [59]. Fig. 7b shows the A-weighted noise distribution of an example tilt-wing aircraft obtained through this method at different ground positions with a hover height of 20m, from with the noise evaluation value of the four noise monitoring points can be easily obtained. As an approximation approach, this method ignores the influence of the noise of secondary components such as motors, fuselage, and wings, but it still provides an effective reference for the comparison of propeller shape, number, sizes, and operating conditions between different design samples.

E. WING WEIGHT

The wing weight generally accounts for 25% to 30% of the total structural weight, or 7.5%-12% of the total take-off weight for the traditional fixed-wing aircraft [60]. The difference in wing weight in different designs directly affects the payload and fuel carried, thereby significantly affecting the overall performance of the design sample. There are many

factors that affect the wing weight, such as the wing shape, load magnitude and distribution, etc. For example, an increase in aspect ratio will result in an increase in wing weight for a constant wing load and wing area, whereas the transition from a centralized load to a distributed load will effectively reduce the wing weight.

In this study, the engineering beam method [61] was used to evaluate the effect of the wing shape and load distribution on the wing weight. The method calculates the wing weight by evaluating the mass of the main load-bearing wing box. The critical state of the main load-bearing wing box is the damage caused by the wall compression failure or the skin instability. To reduce the wing weight, the main load-bearing wing box can be made by the composite materials with high specific strength and specific modulus (such as the T700 carbon fiber prepreg). During the mission, the main forces exerted on the wing include the thrust and normal force of the propellers/rotors, distributed aerodynamic force, the gravity of the power unit, etc. The specific forms of these forces are significantly different in different flight status, as shown in Fig. 8. The upper and lower flanges and the webs of the main load-bearing wing box are (±45/0) layered to bear the multi-directional bending moments caused by the forces in Fig. 8, as well as the shear flow caused by shear forces and torques.

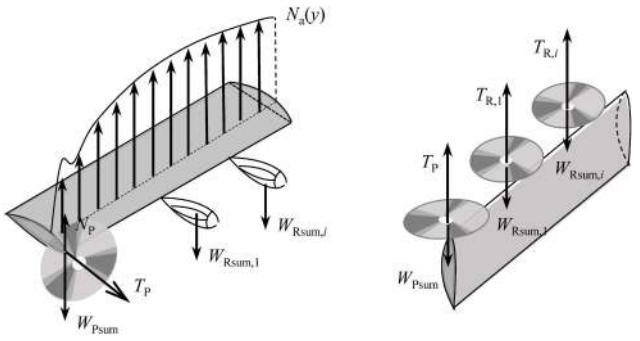

(a) Fixed-wing cruise (b) Rotor-mode hovering (state 1)

FIGURE 8. The force on the wing under different working conditions, where N_a represents the aerodynamic load. T_P represents the thrust of propeller, and T_R the rotor. W_{Psum} represents the total mass of electric drives and propeller set, whereas W_{Rsum} the total mass of electric drives and rotor set. N_P is the propeller normal force.

With propeller/rotor thrust and normal force output by the oblique inflow BEMT method and the aerodynamic load distribution under propeller/rotor wake determined by the nonlinear VLM, the values of the shear force F_s, bending moment M_b, and torque M_t of the wing can be generated along the span. The main load-bearing wing box mass is equal to the sum of the shear structure mass, bending structure mass, and torsion structure mass, as follows:

$$M_{W,main} = 2\int_0^{b/2} (\bar{m}_{shear}(y) + \bar{m}_{bend}(y) + \bar{m}_{tor}(y))dy \tag{11}$$

where $\bar{m}_{shear}$, $\bar{m}_{bend}$, $\bar{m}_{tor}$ represent the mass per unit length of the shear, bending, and torsion structure. Selecting the fixed-wing cruise and rotor-mode hovering state under extreme load to analyze the wing weight yields the calculation formula of $\bar{m}_{shear}$, $\bar{m}_{bend}$, $\bar{m}_{tor}$ as follows [61]:

$$\bar{m}_{shear}(y) = \sum_{i=1,2} n_s k_s \frac{\rho_c F_{s,i}(y)}{\sigma_s} \tag{12}$$

$$\bar{m}_{bend}(y) = \sum_{i=1,2} n_s \rho_b w_i(y) t_i(y) \varepsilon \left(\frac{M_{b,i}(y)}{w_i(y) t_i(y)^2 E}\right)^e \tag{13}$$

$$\bar{m}_{tor}(y) = \sum_{i=1,2} n_s k_s \frac{\rho_c M_{t,i}(y)[w_i(y) + t_i(y)]}{\sigma_s w_i(y) t_i(y)} \tag{14}$$

where the subscript $i = 1$ represents the cruising state and $i = 2$ the hovering state; ρ_c and ρ_b are the density of the shear and bending materials, respectively. σ_s is the allowable shear stress, E the elastic modulus, k_s the shear instability factor. ε and e represent the compression instability factor and the instability index, respectively; $w(y)$ is the width distribution of the bearing wing box while $t(y)$ the corresponding height distribution; n_s is the material safety margin considering the extreme load. The secondary weight including the ribs and rudder surface, and the adhesive mass are regarded to be proportional to the main load-bearing wing box mass, where the proportional coefficients are recorded as k_{sec} and k_{glue} [62], and are selected according to the actual manufacturing level. Summing up the main load-bearing box mass, the secondary mass, and the adhesive mass yields the total weight of the wing.

F. OTHER WEIGHT

In addition to the wing weight, the total take-off weight of the tilt-wing aircraft also includes other structural mass (including the tilt mechanism), the avionics mass, the power system mass, and the payload mass. During the system-level optimization, the power system mass and the wing mass is relatively sensitive to design parameters, whereas other structural mass and avionics mass usually have no significant change. Therefore, at the initial design stage, the mass of other structures except the wing mass can be generally taken as 20%-32.5% of the total take-off mass, whereas the avionics mass taken as 6%-8% [60].

The power system of the tilt-wing aircraft mainly includes batteries, electric drives (motors and electronic speed controllers), propellers/rotors, etc. Among them, the electric drive mass and propeller/rotor mass are determined by the corresponding maximum design power. The output power of the electric drives in the given flight state is equal to the propeller/rotor absorbed power calculated by the BEMT method, and the maximum value of the propeller/rotor absorbed power in all flight conditions is equal to the maximum design power of the two components. The mass of the electric drives with known maximum design power is calculated by (15). The equation is derived from the statistical data of large amounts of existing products with $R^2 = 0.97$, and corrected by the

method proposed by Gundlach to consider the impact of voltage change from the reference maximum voltage $U_{\mathrm{ED0,max}}$ to the actual maximum voltage $U_{\mathrm{ED,max}}$. The propeller/rotor mass is calculated using the approach proposed Roskam [63] based on the known blade number N_{b}, blade diameter D_{PR} and the maximum absorbed power $P_{\mathrm{PR,max}}$, as shown in (16).

$$M_{\mathrm{ED}} = 0.158\left(U_{\mathrm{ED,max}}/U_{\mathrm{ED0,max}}\right)^{0.1588} P_{\mathrm{ed,max}} + 0.024\left(P_{\mathrm{ed,max}} + 1.3096\right) \quad (15)$$

$$M_{\mathrm{PR}} = 0.0586 N_{\mathrm{b}}^{0.391}\left(D_{\mathrm{PR}} P_{\mathrm{PR,max}}\right)^{0.782} \quad (16)$$

The battery output power under the i-th flight stage, $P_{\mathrm{batt},i}$, is equal to the total output power of all electric drives (i.e., $\Sigma P_{\mathrm{ED},i}$) divided by the electric drive efficiency η_{ED}, whereas the battery consumed energy $E_{\mathrm{batt},i}$ is equal to the product of $P_{\mathrm{batt},i}$ and the duration t_i, i.e., $E_{\mathrm{batt},i} = P_{\mathrm{batt},i} t_i$. Therefore, the overall battery mass under the dual constraints of power and energy can be expressed as:

$$M_{\mathrm{batt}} = \max\left(\frac{\max\left(P_{\mathrm{batt},1}, P_{\mathrm{batt},2}, \ldots\right)}{\rho_{\mathrm{batt,P}}}, \frac{\sum_{i=1}^{5} E_{\mathrm{batt},i}}{\rho_{\mathrm{batt,E}}}\right) \quad (17)$$

where $\rho_{\mathrm{batt,P}}$ and $\rho_{\mathrm{batt,E}}$ represent the battery power density and energy density, respectively.

G. SECONDARY AERODYNAMIC FORCE

Other components besides the wing (including the horizontal tail, vertical tail, fuselage, etc.) also have some important influences on the overall aircraft aerodynamic evaluation. Among them, the horizontal tail aerodynamics can be evaluated in the same way as the wing aerodynamic evaluation, but a downwash angle is required to be added to the incoming flow to account for the wing-tail interference [64]. Vertical tail usually does not contribute to the lift and pitch moments, but its drag cannot be neglected. The vertical tail drag D_{vt} is mainly the zero-lift drag, that is, $D_{\mathrm{vt}} = C_{\mathrm{D0,vt}} q S_{\mathrm{vt}}$, where S_{vt} is the vertical tail area, q is the dynamic pressure, and $C_{\mathrm{D0,vt}}$ is the vertical tail's zero-lift drag coefficient. Fuselage drag consists of zero-lift drag and lift-induced drag. For the non-lifting fuselages, the latter item is usually negligible, whereas the zero-lift drag coefficient $C_{\mathrm{D0,F}}$ is calculated using the following formula [65]:

$$C_{\mathrm{D0,F}} = R_{\mathrm{WF}} C_{\mathrm{fF}}\left[1 + 60/\left(\frac{l_{\mathrm{F}}}{d_{\mathrm{F}}}\right)^3 + 0.0025\left(\frac{l_{\mathrm{F}}}{d_{\mathrm{F}}}\right)\right]\frac{S_{\mathrm{wetF}}}{S} \quad (18)$$

where R_{WF} is the wing-fuselage interference factor, C_{fF} is the friction coefficient of the turbulent flat surface, l_{F} the fuselage length, d_{F} the maximum fuselage diameter, S_{wetF} the fuselage wet area, and S the wing reference area. Superimposing the above-mentioned secondary aerodynamic forces and the wing aerodynamic forces completes the evaluation of the overall aerodynamic characteristics of the tilt-wing aircraft.

III. OPTIMIZATION PROCESS

A. OPTIMIZATION GOAL

The utility of the tilt-wing cargo aircraft can be evaluated in two indicators - the delivery efficiency and delivery cost. Delivery efficiency represents the average mass of the cargo transported per unit hour (Unit: kg/h), which is calculated by

$$J_\eta = \frac{V_{\mathrm{cru}} M_{\mathrm{cargo}}}{D_{\mathrm{cargo}}} = \frac{V_{\mathrm{cru}}}{D_{\mathrm{cargo}}} \times \left(M_{\mathrm{TO}} - M_{\mathrm{wing}} - M_{\mathrm{otherStr}} - M_{\mathrm{P}} - M_{\mathrm{ae}}\right) \quad (19)$$

where V_{cru} represents cruise speed, M_{cargo} the cargo mass, M_{wing} the wing mass, M_{otherStr} other structural mass, M_{P} power system mass, M_{TO} the total take-off mass, and D_{cargo} the delivery distance. For a given delivery distance, the faster the cruise speed and the heavier the cargo carried, the higher the delivery efficiency. As can be seen from (19), measures helpful to improve the delivery efficiency include increasing the cruising speed V_{cru}, reducing the wing mass, reducing the power system mass, etc.

Delivery cost, on the other hand, is an important economic indicator in the freight profile, which represents the electricity consumed per unit mass cargo (Unit: kWh/kg), and calculated by

$$J_{\mathrm{cost}} = \frac{1}{M_{\mathrm{cargo}}}\left(\frac{P_{\mathrm{batt,cru}} D_{\mathrm{cargo}}}{V_{\mathrm{cru}}} + P_{\mathrm{batt,hv}} E_{\mathrm{hv}}\right) = \frac{c_0}{M_{\mathrm{cargo}}}\left(\frac{c_1}{(L/D)\,\eta_{\mathrm{P}}} + \frac{c_2}{\delta_{\mathrm{DEP}}}\right) \quad (20)$$

where $c_0 = D_{\mathrm{cargo}} M_{\mathrm{TO}} g$, $c_1 = 1/\eta_{\mathrm{ED}}$, $c_2 = E_{\mathrm{hv}}/(\eta_{\mathrm{ED}} D_{\mathrm{cargo}})$. $P_{\mathrm{batt,hv}}$ represents the battery output power in hovering state and $P_{\mathrm{batt,cru}}$ in fixed-wing cruise state. E_{hv} represents the hovering duration, g the acceleration of gravity. L/D is the cruising-state lift-drag ratio of the tilt-wing aircraft. η_{P} represents the propeller efficiency in cruising state, δ_{DEP} represents the overall thrust efficiency of all propellers and rotors in DEP during hovering (state 1), whereas η_{ED} the electric drive efficiency. The above formula shows that the cruising speed has no impact on the delivery cost, and the main measure to reduce the delivery cost is to increase the values of M_{cargo}, L/D, η_{P}, and δ_{DEP}.

B. DESIGN PARAMETERS

In this study, the parameters used for the tilt-wing cargo unmanned aircraft optimization can be divided into three categories, namely the wing design parameters $\boldsymbol{\psi}_{\mathrm{wing}}$, DEP design parameters $\boldsymbol{\psi}_{\mathrm{DEP}}$, and operation control parameters $\boldsymbol{\psi}_{\mathrm{c}}$. Among them, the wing design parameter $\boldsymbol{\psi}_{\mathrm{wing}}$ equals to $\{S_{\mathrm{w}}, \chi_{\mathrm{w}}, \zeta_{\mathrm{w}}, b_{\mathrm{w}}, \theta_{\mathrm{w}}\}$, where S_{w} is the wing reference area, χ_{w} the sweep angle, ζ_{w} the tip root ratio, b the wingspan, and θ_{w} the wing installation angle. DEP design parameter $\boldsymbol{\psi}_{\mathrm{DEP}}$ equals to $\{D_{\mathrm{P}}, D_{\mathrm{R}}, N_{\mathrm{R}}, N_{\mathrm{b}}^{\mathrm{P}}, N_{\mathrm{b}}^{\mathrm{R}}, \boldsymbol{p}_\theta^{\mathrm{P}}, \boldsymbol{p}_c^{\mathrm{P}}, \boldsymbol{p}_\theta^{\mathrm{R}}, \boldsymbol{p}_c^{\mathrm{R}}\}$, where D_{P} represents the diameter of the wingtip propeller, D_{R} the rotor diameter, N_{R} the rotor number. $N_{\mathrm{b}}^{\mathrm{P}}$ represents the blade number of the propeller while $N_{\mathrm{b}}^{\mathrm{R}}$ that of the rotor. $\boldsymbol{p}_\theta^{\mathrm{P}}, \boldsymbol{p}_c^{\mathrm{P}}, \boldsymbol{p}_\theta^{\mathrm{R}}, \boldsymbol{p}\mathrm{R}\ c$ are the characteristic coefficient sets in the

fourth-order Bezier curve used to describe the distribution of propeller/rotor chord length and twist angle [66], e.g., $\boldsymbol{p}_{\theta}^{\mathrm{P}} = [p_{0,\theta}^{\mathrm{P}}, p_{1,\theta}^{\mathrm{P}}, p_{2,\theta}^{\mathrm{P}}, p_{3,\theta}^{\mathrm{P}}, p_{4,\theta}^{\mathrm{P}}]$, $\boldsymbol{p}_{\mathrm{c}}^{\mathrm{P}} = [p_{0,\mathrm{c}}^{\mathrm{P}}, p_{1,\mathrm{c}}^{\mathrm{P}}, p_{2,\mathrm{c}}^{\mathrm{P}}, p_{3,\mathrm{c}}^{\mathrm{P}}, p_{4,\mathrm{c}}^{\mathrm{P}}]$, as shown in (21). The operation control parameter $\boldsymbol{\psi}_{\mathrm{c}}$ equals to $\{\Phi, Ma_{\mathrm{cr}}^{\mathrm{P}}, Ma_{\mathrm{cr}}^{\mathrm{R}}\}$, where Φ is the thrust allocation ratio between the wing-mounted propellers and rotors, $Ma_{\mathrm{cr}}^{\mathrm{P}}$ and $Ma_{\mathrm{cr}}^{\mathrm{R}}$ represent the blade tip Mach number of the propellers and the rotors during the minimum speed flight (state 5), respectively.

$$\begin{aligned} \theta_{\mathrm{P}}(r) &= \sum_{i=0}^{4} p_{i,\theta}^{\mathrm{P}} (1-r)^i r^i \\ c_{\mathrm{P}}(r) &= \sum_{i=0}^{4} p_{i,\mathrm{c}}^{\mathrm{P}} (1-r)^i r^i \end{aligned} \tag{21}$$

For the unmanned tilt-wing aircraft performing a cargo-delivery task, the typical ranges of the above parameters are listed in Table 2, in which, S_0 is the wing area benchmark determined by the takeoff weight and typical wing loading (50-60 kg/m2 for the unmanned cargo aircraft), and b_0 is the upper limit of the wingspan which is determined by the allowable space at the takeoff and landing sites.

TABLE 2. Range of design parameters.

Parameter	Range	Parameter	Range
S_{w} (m^2)	$0.6S_0$- S_0	N_{R}	2-8
χ_{w} (°)	0-20	$N_{\mathrm{b}}^{\mathrm{P}}$	2-6
ζ_{w}	0.4-1	$N_{\mathrm{b}}^{\mathrm{R}}$	2-6
b_{w} (m)	$0.5b_0$- b_0	$p_{i,\theta}^{\mathrm{P}}$, $p_{i,\theta}^{\mathrm{R}}$	-15-30
θ_{w} (°)	-1-3	$p_{i,\mathrm{c}}^{\mathrm{P}}$, $p_{i,\mathrm{c}}^{\mathrm{R}}$	-0.5-3
D_{P} (m)	$0.1b_{\mathrm{w}}$-$0.4b_{\mathrm{w}}$	Φ	0-0.8
D_{R} (m)	$0.1b_{\mathrm{w}}$-$0.4b_{\mathrm{w}}$	$Ma_{\mathrm{cr}}^{\mathrm{P}}$, $Ma_{\mathrm{cr}}^{\mathrm{R}}$	0.1-0.7

In addition to the above parameters, the complete description of the tilt-wing aircraft should also cover the tail-mounted rotor, tail, and fuselage. The tail-mounted rotors are used to balance the aircraft in rotor mode. The number and disk load are kept constant, but the diameter is adjusted based on the selection of the wing-mounted propeller/rotor design parameters. The fuselage geometric parameters, the vertical tail geometric parameters, and the wing/tail installation position are preset, and do not change during the optimization process. Special attention should be given to the design parameters of the horizontal tail, whose basic geometry is fixed but the area and installation angle is adjusted using the least drag principle based on the trimming requirement during the cruise state.

C. CONSTRAINTS

Constraints that need to be met during the optimization design process include the following: 1) Flight safety constraints: The overall forces and moments on the aircraft in each flight state is required to meet the safe operation demand, that is, $F_{\mathrm{x}} \geq 0$, $F_{\mathrm{z}} \geq 0$, $M_{\mathrm{y}} = 0$; 2) Space interference constraint: The distance between the tips of propellers and rotors is required to be greater than 0.1 times the propeller/rotor radius; 3) Blade tip Mach number constraint: The tip Mach number of each propeller/rotor does not exceed 0.7 in any operating state; 4) Cargo mass constraint: The cargo mass must be positive; 5) Noise constraint: The average noise under hovering state must be lower than the given threshold.

D. OPTIMIZATION IMPLEMENTATION

The proposed optimization problem can be summarized as in (22), where m is the design space dimension, $\boldsymbol{X}$ is the collection of solutions that satisfy all constraints. Based on the mathematical and physical model described in Section II, a detailed process to solve the problem is constructed, as shown in Fig. 9. This process includes five major parts, namely the global preprocessing, sample preprocessing, operating state analysis, utility evaluation, and genetic algorithm optimization.

$$\begin{aligned} V-\min \boldsymbol{J}\left(\boldsymbol{\psi}_{\mathrm{wing}}, \boldsymbol{\psi}_{\mathrm{DEP}}, \boldsymbol{\psi}_{\mathrm{c}}\right) &= \left[J_{\eta}, -J_{\mathrm{cost}}\right]^{\mathrm{T}} \\ \text{s.t. } [\boldsymbol{\psi}_{\mathrm{wing}}, \boldsymbol{\psi}_{\mathrm{DEP}}, \boldsymbol{\psi}_{\mathrm{c}}] &\in \boldsymbol{X} \\ \boldsymbol{X} &\subseteq \boldsymbol{R}^m \end{aligned} \tag{22}$$

The global pre-processing only runs once during the entire optimization process. Its main functions include 1) assigning the top-level design requirements to each boundary operating state, 2) establishing the viscous aerodynamic database for the wing airfoil and propeller/rotor airfoil under different Reynolds numbers, 3) establishing the trim database for the horizontal tail with the different tail area and installation angles using the nonlinear VLM.

The sample pre-processing part is executed for each design sample, which adaptively generates the wing calculation grid, and converts the propeller/rotor design parameters into the detailed chord length and torsion angle distribution.

Operating state analysis is the major part of the optimization process, which is use to 1) determine the cruise speed, the tail area and installation angle according to the VLM results in the cruise state; 2) solve the cruise-state propeller rotatory speed and aerodynamics using oblique BEMT method and Newton iteration method; 3) recalculate the wing load distribution with propeller slipstream as necessary input, and update the propeller-absorbed power; 4) solve the propeller/rotor rotatory speed and corresponding aerodynamics in states 1, 2, 3, 4 according to the trim requirements using oblique BEMT method, Newton iteration method, and nonlinear VLM; 5) solve the propeller/rotor slipstream distribution in state 5 with given propeller/rotor blade tip Mach, and calculate the lift distribution on the wing with nonlinear VLM, and output the overall lift coefficient; 6) determine the powertrain power and mass using the propeller/rotor absorbed power obtain in each flight state, and calculate the wing mass using the wing engineering beam method.

The utility evaluation is used to conduct the noise monitoring, stall judgement, and to complete the final evaluation of the delivery efficiency and delivery cost. The calculation

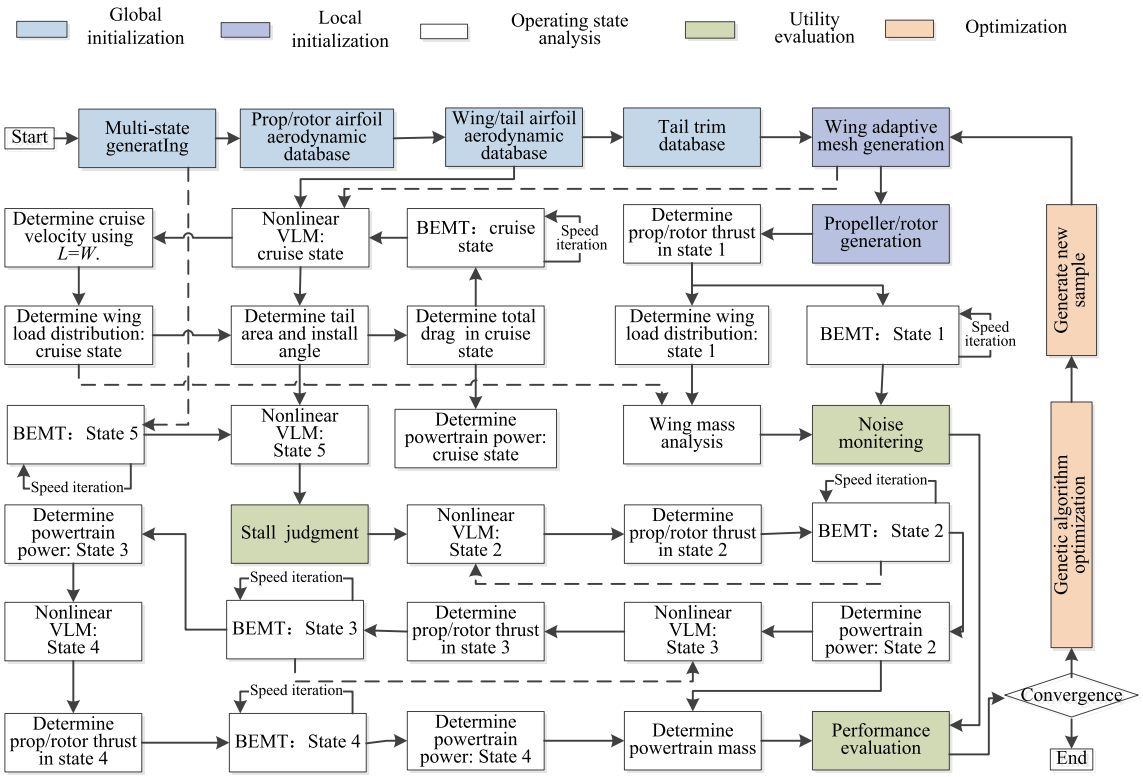

FIGURE 9. Optimization implementation process.

samples are initially set by the Latin hypercube method [67] and then updated using the multi-objective genetic algorithm (MOGA) [68]. The design constraints are checked at each calculation step. When the historical best utility value converges, the optimal design is obtained.

IV. CASE STUDY

In this section, the optimization of a 200-kg tilt-wing cargo aircraft was carried out using the method proposed. The aircraft is used to perform a 100-km cargo distribution task. The specific factors affecting the optimization results are studied. The detailed mechanism by which these factors affect the results is also discussed.

A. DESIGN REQUIREMENTS

The tilt-wing cargo aircraft studied herein is equipped with two sets of wingtip propellers, two sets of tail rotors, and N_R sets of rotors ($N_R = 2, 4, 6, 8, \ldots$), which is used to perform the rapid delivery task from the central warehouse to the regional distribution center. The total take-off mass is 200kg, the delivery distance is 100kM, the cruising altitude is 150m, and the maximum hover duration is set as 5 minutes. The wing of the aircraft adopts GAW-1 airfoil, the tail adopts NACA 0012, and the propeller/rotor adopts the NACA 16-series airfoils. To reduce the number of design parameters, the wing is set as a straight wing without swept back, and the wingspan is limited to 8m to meet the landing site restrictions. The flaps are placed on the inside of the wing, which accounts for 50% and 25% in wingspan and wing chord, respectively, and the flap declination is set as 20° in state 5. Table 3 lists the aircraft performance requirements in each flight mode (FW: Fix-wing; RT: Rotor; TS: Transition). Other input parameters can be found in Table 4.

TABLE 3. Design requirements in each flight mode.

Design requirement	Unit	Value
RT mode: hovering duration	min	3.5
FW mode: Minimum speed	m/s	20
FW mode: Cruise altitude	M	150
FW mode: Maximum speed	m/s	45
TS mode: Cessation speed	m/s	25

TABLE 4. Other input parameters.

Input parameter	Unit	Value
Avionics mass fraction	-	0.08
Other structural mass fraction	-	0.25
Electric drive maximum voltage	Volt	315
Electric drive efficiency	-	80%
Battery power density	W/kg	2000
Battery energy density	Wh/kg	250

B. OPTIMIZATION RESULTS

Based on the optimization process illustrated in Fig. 9, the design optimization of the tilt-wing cargo aircraft was carried out with $N_R = 2$, 4, 6, and 8, respectively. The parameters

TABLE 5. The values of optimal design variables and the corresponding main performance.

Item	N_R=2		N_R =4		N_R =6		N_R =8	
	DEP OFF	DEP ON	DEP OFF	DEP ON	DEP OFF	DEP ON	DEP OFF	DEP ON
Wing area (m^2)	4.09	3.71	4.09	3.45	4.09	3.27	4.09	3.18
Propeller diameter (m)	1.58	1.79	1.61	1.35	1.48	1.50	1.57	1.67
Propeller blade number	2.00	2.00	2.00	2.00	2.00	2.00	2.00	2.00
Rotor diameter (m)	2.47	2.37	1.25	1.31	0.86	0.86	0.64	0.63
Rotor blade number	4.00	4.00	4.00	4.00	4.00	4.00	3.00	4.00
Propeller blade tip Mach in State 5	-	0.38	-	0.31	-	0.20	-	0.13
Rotor blade tip Mach in State 5	-	0.34	-	0.42	-	0.40	-	0.49
Thrust allocation ratio	0.75	0.71	0.75	0.78	0.71	0.71	0.60	0.70
Tail area (m^2)	0.7	0.66	0.7	0.63	0.7	0.60	0.7	0.62
Tail installed angle (°)	1.0	1.0	1.0	1.0	1.0	1.0	1.0	1.0
Tail rotor diameter (m)	0.481	0.48	0.481	0.481	0.48	0.481	0.481	0.482
Cruise speed (m/s)	29.93	31.16	29.92	32.08	29.89	32.85	29.93	33.35
Wing lift-drag ratio	30.58	33.32	30.68	35.76	30.64	37.23	30.66	37.91
Overall lift-drag ratio	14.42	14.36	14.44	14.30	14.44	14.13	14.42	13.98
Propeller efficiency	80.7%	81%	80.9%	80.8%	80.2%	80.1%	80.5%	81.1%
Overall thrust efficiency (kg/kw)	6.7	6.71	6.04	6.06	5.21	5.22	4.25	4.24
Delivery efficiency (kg/h)	43.66	51.74	46.38	52.84	41.17	52.79	43.38	48.97
Delivery cost (kwh/kg)	0.362	0.303	0.331	0.312	0.391	0.335	0.369	0.364
Noise (dB)	61.90	60.30	61.44	62.76	62.88	63.15	60.07	64.29

of the MOGA were set to the same in each case, in which the initial population size was set to 200, the crossover rate was set to 0.8, the mutation rate was set to 0.03, and the maximum evolutionary generation was set to 200. The corresponding DEP-off cases that neglect the slipstream effect were selected as a control group to show the impact of DEP. The optimization processes are presented in Fig. 10, whereas the optimization results are shown in Table 5, Fig. 11, and Fig. 12. Significant differences can be found in both design parameters and aircraft performance between the DEP-open cases and DEP-off cases. With DEP turned on, the wing area can be reduced by 9.1%, 15.6%, 19.9%, 22.3% for $N_R = 2, 4, 6$, and 8, respectively, whereas the cruise speed increased by 4.1%, 7.2%, 9.9%, 11.4%, delivery efficiency increased by 18.5%, 13.9%, 28.2%, 12.9%, and Delivery cost reduced by 15%, 4.7%, 13.9%, and 1.3%. The results fully prove the application potential of DEP in improving delivery efficiency and decreasing delivery costs.

However, the DEP benefit is also different for the four DEP-on cases, in which the delivery cost is sorted by $J_{cost}^{N_R=2} < J_{cost}^{N_R=4} < J_{cost}^{N_R=6} < J_{\text{cost}}^{N_R=8}$, the delivery efficiency is sorted by $J_{\eta}^{N_R=8} < J_{\eta}^{N_R=2} < J_{\eta}^{N_R=6} < J_{\eta}^{N_R=4}$, whereas the noise level is sorted by $N_{\text{dB}}^{N_R=2} < N_{\text{dB}}^{N_R=4} < N_{\text{dB}}^{N_R=6} < N_{\text{dB}}^{N_R=8}$. The delivery cost and noise are both lowest when $N_R = 2$, but the delivery efficiency is the highest when $N_R = 4$. However, the performance differences between the two cases are relatively small (within 3%), so both can be taken as the final optimized design scheme.

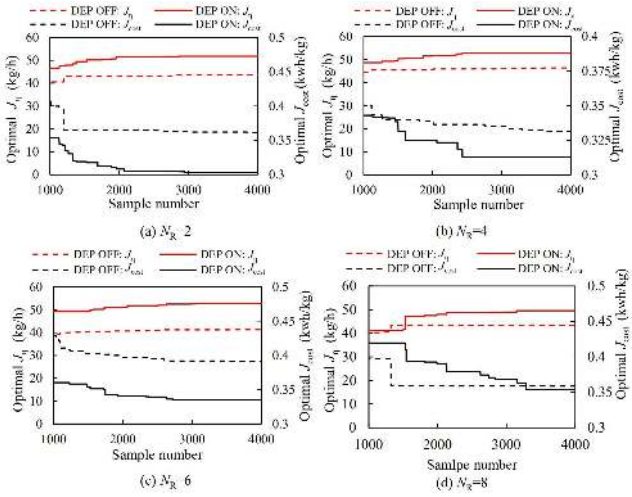

FIGURE 10. Optimization process.

C. ANALYSIS AND DISCUSSION

In this section, a detailed analysis of the preceding calculation examples is performed to reveal the reasons for these results and find out the design principles of the tilt-wing cargo aircraft using DEP system.

1) DRAG REDUCTION CAUSED BY WINGTIP PROPELLER

During the fixed-wing flight, the wingtip vortex generated by the pressure difference between the upper and lower wing

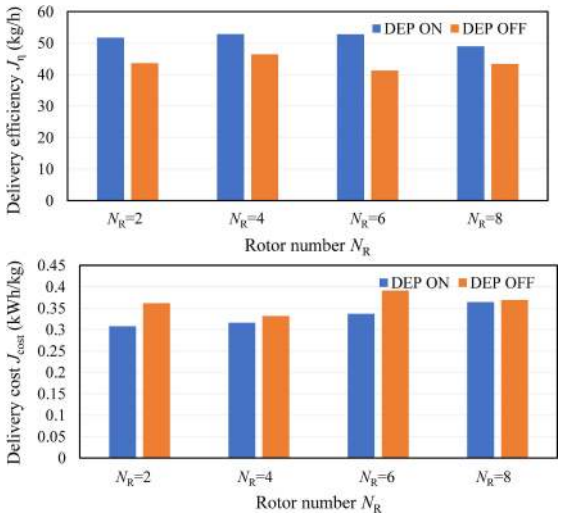

FIGURE 11. Optimization results: Comparison between DEP-on and DEP-off cases.

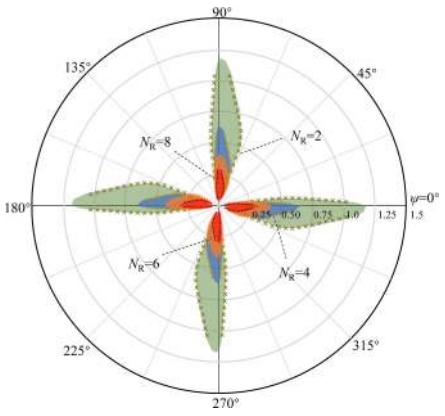

FIGURE 12. Optimization results: rotor chord distribution determined by fourth-order Bezier curves. For example, in DEP-on cases, when $N_R = 2$, $p_c^R = [-0.0066, 0.0287, 0.233, 0.0453, 0.0575]$. Twist angle distribution is optimized in the same way, though not presented.

surfaces is an important source of induced drag. The wingtip propeller can effectively suppress the vortex by inboard-up rotation, thereby effectively reducing the induced drag. The propeller slipstream can also increase the wingtip dynamic pressure, and thus can increase the lift. Such aerodynamic benefit can be found in all optimized design results, as shown in Fig. 13. Compared with the propeller-off state, when the wingtip propeller is turned on, the wing lift-drag ratio is increased by 5.77%, 6.65%, 6.2%, 5.43% for $N_R = 2$, 4, 6, 8, respectively, whereas the lift-drag ratio of the entire aircraft increased by 2.93%, 3.35%, 2.94% and 2.37%. The rotating speed, thrust, and absorbed power of the propeller is determined by the drag during cruise flight, so the above aerodynamic benefit can be achieved without additional power, which is of great significance for improving cruise efficiency.

2) LIFT INCREASE CAUSED BY DEP WAKE

In the minimum-speed flight state, propellers and rotors in DEP are operated at the specified speed set by the input

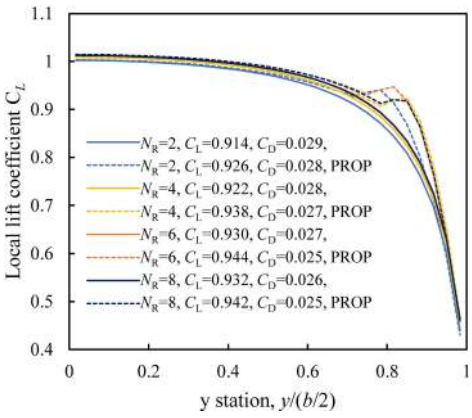

FIGURE 13. Local C_L distribution along the wingspan in cruise state.

blade-tip Mach number. The axis flow of the propeller/rotor wake greatly accelerates the airflow on the upper and lower wing surfaces, increases the incoming dynamic pressure, whereas the tangential flow changes the inflow angle of attack. The nonlinear VLM results illustrate that the interaction of wake and wing has some obvious benefit for the lift increase, as shown in Fig. 14. The wake-induced lift increase is highest (25.6%) when $N_R = 8$, and gradually weakened as N_R decreases, which is 22.3%, 16.7%, and 9.1% for $N_R = 6$, 4, and 2, respectively. The dynamics pressure increase is the dominant factor for the increase in wake-induced lift. Theoretically, the dynamics pressure at small N_R can be further increased, but due to the larger disk area, the slipstream field is more dispersed compared with that at high N_R, which means the price paid (i.e., power) to increase the dynamic pressure is high that may lead to the rapid deterioration in delivery efficiency and delivery costs. In contrast, small-diameter DEP with high N_R is more efficient in wake generation, which is also why the DEP on fixed-wing aircraft like NASA X-57 takes a small diameter.

The wake-induced lift increase in minimum-speed flight (state 5) reduces the wing size required for safe flight, and induces some changes in cruise state and lift-drag characteristics, as shown in Fig. 15. For a given wingspan, a smaller wing area corresponds to a larger wing aspect ratio AR (i.e., $AR = 17.2$ for $N_R = 2$, $AR = 20.2$ for $N_R = 8$), which also means a larger wing lift-to-drag ratio and smaller wing cruise drag. However, to maintain the aircraft balance with a smaller wing area in the cruise state, higher cruise speed is required. Such a higher cruise speed will bring a significant increase to the drag of the non-lifting components (such as the fuselage and vertical tail, which contributes 60% of the total drag), and will inhibit the benefit of wing lift-to-drag ratio improvement on the overall aircraft aerodynamics. For the above reason, although the wing drag at $N_R = 2$ is 12% lower than that at $N_R = 8$, the total aircraft drag is 2.7% higher.

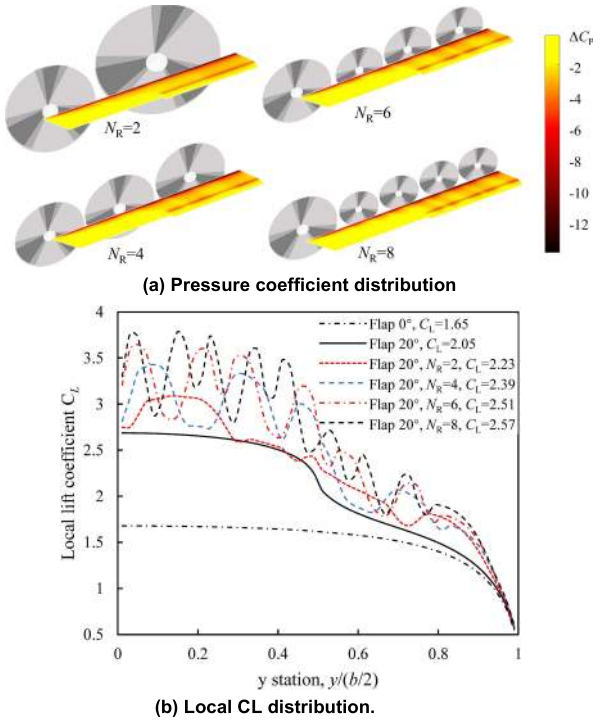

(a) Pressure coefficient distribution

(b) Local CL distribution.

FIGURE 14. Waked wing aerodynamic characteristic in state 5.

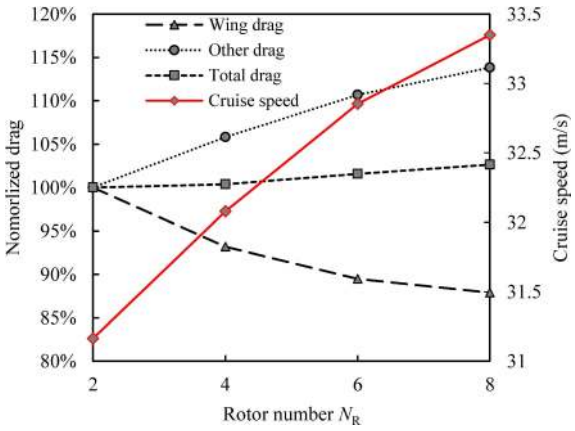

FIGURE 15. Comparison in cruise speed and cruise aerodynamic characteristics at $N_R = 2$, 4, 6, and 8. All drag values are divided by the corresponding drag in the $N_R = 2$ case to normalize.

3) IMPACT OF DEP ON POWER SYSTEM DESIGN

To reduce the maximum design power and mass of power system, the propeller/rotor thrust efficiency should be improved as much as possible under high-power demand states like states 1, 2, 3. The DEP scheme with high N_R has an absolute advantage in the lift increase in state 5, but is at an absolute disadvantage in thrust efficiency during the flight in states 1, 2, 3 (see Fig. 16). Although the hovering thrust efficiency and cruise propulsion efficiency of wingtip propellers are close in $N_R = 2$, 4,6, 8 cases, the values of rotor thrust efficiency are significantly different. Such differences are mainly caused by the difference in the rotor diameter. Once the thrust demand is set, the large the rotor diameter, the greater the potential for

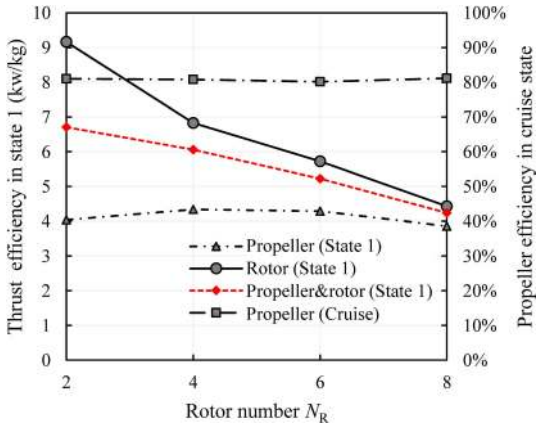

FIGURE 16. Propeller and rotor performance at $N_R = 2$, 4, 6, and 8.

optimization, which means the higher rotor thrust efficiency can be achieved. Since the rotor thrust accounts for more than 70% of the total wing-mounted propeller/rotor thrust, the rotor thrust efficiency order determines the sequence of the overall DEP thrust efficiency ($\eta_{\mathrm{DEP}}^{N_R=2} > \eta_{\mathrm{DEP}}^{N_R=4} > \eta_{\mathrm{DEP}}^{N_R=6} > \eta_{\mathrm{DEP}}^{N_R=8}$). The total mass of electric drives, propellers, and rotors follows the reverse order, which is lightest when $N_R = 2$, and heaviest when $N_R = 8$.

The battery mass is determined by both the power constraint and energy constraint. The order of the battery mass of the four DEP-on cases under power constraint is consistent with the sequence of other power transferring components, i.e., $M_{\mathrm{batt,P}}^{N_R=2} < M_{\mathrm{batt,P}}^{N_R=4} < M_{\mathrm{batt,P}}^{N_R=6} < M_{\mathrm{batt,P}}^{N_R=8}$. The energy-constrained battery mass, on the other hand, is analyzed in two parts: the battery mass corresponding to the energy required in hovering state (state 1) is proportional to the operating power since the operating duration is fixed; the battery mass corresponding to the cruise energy is determined by the propeller propulsion efficiency η_P, aircraft lift-to-drag ratio L/D, electric drive efficiency η_{ED}, and battery energy density $\rho_{\mathrm{batt,E}}$ as in (22). Note that the battery mass required in the cruise state has nothing to do with cruise speed V_{cru}, which is very important.

$$M_{\mathrm{batt,E}}^{\mathrm{cru}} = P_{\mathrm{batt,cru}} t / \rho_{\mathrm{batt,E}} = \frac{W_{\mathrm{TO}} \cdot V_{\mathrm{cru}}}{(L/D)\,\eta_P \eta_{ED}} \frac{D_{\mathrm{cargo}}}{\rho_{\mathrm{batt,E}} V_{\mathrm{cru}}} = \frac{W_{\mathrm{TO}} \cdot D_{\mathrm{cargo}}}{(L/D)\,\eta_P \eta_{ED} \rho_{\mathrm{batt,E}}} \tag{23}$$

Based on the above analysis and the values of η_P (81%, 80.8%, 80.1%, 81.1% for $N_R = 2$, 4, 6, 8, respectively) and L/D (81%, 80.8%, 80.1%, 81.1%), the energy-constrained battery mass is sorted by $M_{\mathrm{batt,E}}^{N_R=2} < M_{\mathrm{batt,E}}^{N_R=4} < M_{\mathrm{batt,E}}^{N_R=6} < M_{\mathrm{batt,E}}^{N_R=8}$. Since this order is consistent with the sequence of the power-constrained battery mass, the overall battery mass is also sorted by $M_{\mathrm{batt}}^{N_R=2} < M_{\mathrm{batt}}^{N_R=4} < M_{\mathrm{batt}}^{N_R=6} < M_{\mathrm{batt}}^{N_R=8}$. In terms of the overall power system design which includes the electric drives, propellers, rotors, and batteries, the $N_R = 2$ scheme is lightest, and $N_R = 8$ heaviest. This result

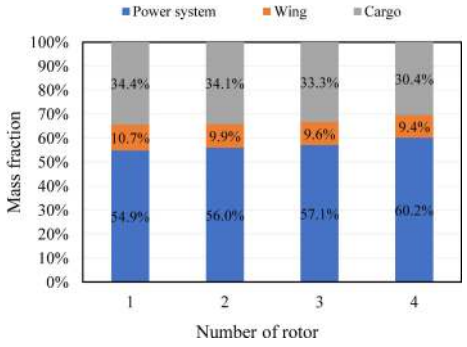

FIGURE 17. The ratio of power system mass, wing mass, and cargo mass to the total mass of the three parts ($N_R = 2$, 4, 6, and 8, DEP-on).

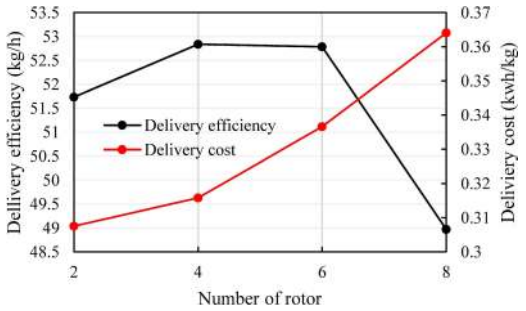

FIGURE 18. Comparison of delivery efficiency and cost at $N_R = 2$, 4, 6, and 8 (DEP-on).

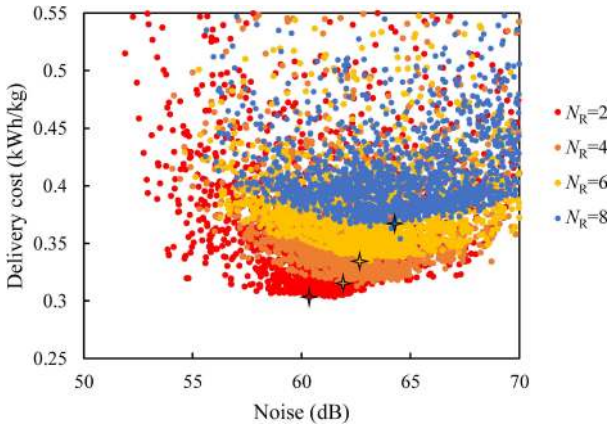

(a) Correspondence between delivery cost and noise. The optimal design results are marked with four-pointed stars.

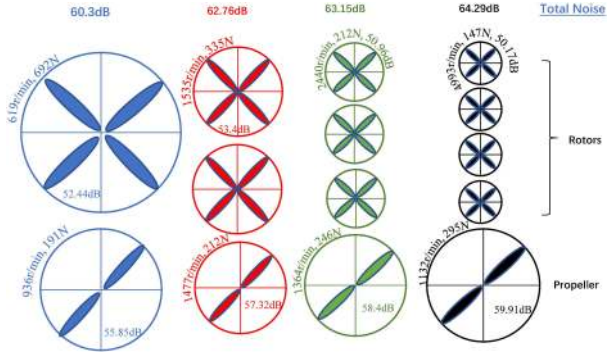

(b) Comparison of the noise level of the four optimal design results.

FIGURE 19. The ratio of power system mass, wing mass, and cargo mass to the total mass of the three parts ($N_R = 2$, 4, 6, and 8).

shows that, benefit from the high DEP efficiency and low overall cruise drag, the design scheme with $N_R = 2$ has the most prominent development advantages in reducing power system mass and energy consumption.

4) IMPACT OF DEP ON WING MASS

The structural mass of the wing is an important factor affecting the utility of tilt-wing cargo aircraft, and it also significantly changes as design parameters vary. Among the four optimized DEP-on schemes, the lightest wing mass is achieved when $N_R = 8$, which is only 87.4% of the wing mass at $N_R = 2$. The values of the wing mass at $N_R = 4$ and $N_R = 6$ locate between the former two, which is 92.1% and 89.6% of the $N_R = 2$ wing mass, respectively. The wing mass reduction caused by the N_R increase is due to the following reasons: 1) The DEP system helps to reduce the load-bearing structural stress in the hovering state (state 1), and the more divergent the DEP (the greater the N_R), the lower the structural stress; 2) For the given external force distribution, the moderate reduction of the chord length plays a positive role in reducing the wing structural mass as in (13), whereas the greater the N_R, the smaller the wing chord length. The above improvement of structural efficiency is another important role of applying the DEP.

5) IMPACT OF DEP ON DELIVERY EFFICIENCY AND COST

According to the definition in (19), delivery efficiency J_η is proportional to cruising speed V_{cru} and cargo mass M_{cargo}, and inversely proportional to delivery distance D_{cargo}. For the four DEP-on schemes, the cruising speed is sorted by $V_{cru}^{N_R=2} < V_{cru}^{N_R=4} < V_{cru}^{N_R=6} < V_{cru}^{N_R=8}$ (see Fig. 15). The order of cargo mass is determined by the power system mass and wing mass, as shown in Fig. 17. The N_R increase helps to improve the wing structural efficiency, but also greatly increases the power system mass, which makes the $N_R = 8$ scheme with highest wing structural efficiency correspond to the lightest M_{cargo}. The final delivery efficiency order depends on the product of V_{cru} and M_{cargo}, as shown by the black line in Fig. 18. The $N_R = 2$ scheme (with the highest M_{cargo} and lowest V_{cru}) and the $N_R = 8$ scheme (with the highest V_{cru} and lowest M_{cargo}) significantly lag the more compromised $N_R = 4$ and $N_R = 6$ schemes in delivery efficiency.

The delivery cost J_{cost} has nothing to do with the cruise speed. It is inversely related to the cargo mass M_{cargo}, the cruise lift-to-drag ratio L/D, the propeller propulsion efficiency η_P, and the overall DEP thrust efficiency η_{DEP}.

The delivery efficiency J_η can be improved by reducing the wing area and increasing cruise speed, but the only way to improve the delivery cost is to increase L/D, η_P, and η_{DEP}. Considering the order of L/D, η_P, and η_{DEP}, the delivery cost is the highest when $N_R = 8$ and the lowest when $N_R = 2$.

6) IMPACT OF DEP ON NOISE

The increase of N_R in the DEP system has an adverse effect on the overall noise level of the optimal design point, as shown in Fig. 19. The noise of the optimal design point is about 60.3dB when $N_R = 2$, and increases to 64.29dB for $N_R = 8$. This rule is very different from the application experience of DEP for the noise reduction in the field of fixed-wing aircraft.

The main reason for this difference is that the DEP applied for fixed-wing aircraft is only used to generate the wake during minimum-speed flight. The larger the N_R, the smaller the rotor disk, and the higher the efficiency of slipstream generation, so the absorbed power and noise for the same level of slipstream can be greatly reduced. However, the tilt-wing aircraft case is very different. In addition to generating the wake, the DEP in tilt-wing aircraft should also meet the high thrust requirements in states 1, 2, 3. The greater the N_R, the lower the thrust efficiency, which increases the absorbed power and rotatory speed of propellers and rotors to produce the same thrust, and the noise increases consequently. Therefore, the noise level also constitutes an important constraint for the upper limit of the rotor number in the DEP during the tilt-wing cargo aircraft optimization.

V. CONCLUSION

In this work, an aerodynamic, propulsion, noise, weight integrated optimization design method was established for the emerging unmanned distributed-propulsor-equipped tilt-wing cargo aircraft. The method consists of a series of mathematical-physical models specially developed or adjusted for the new aircraft, which can comprehensively consider the impact of the propeller/rotor optimization, noise evaluation, propeller/wing interference, and aerodynamic/structure coupling on the design process at the initial stage, thereby translating the top-level design requirements into the optimal design parameters.

The case study reveals the significant impact of the above-mentioned factors on the design results and the importance to comprehensively consider aerodynamic, propulsion, noise, weight control at the initial design stage. The optimization result shows that the DEP and wing interaction provides the possibility to further improve the performance of the unmanned tilt-wing cargo aircraft. Compared with the DEP-off state, when DEP is turned on, the delivery efficiency can be increased by up to 28.2%, whereas the delivery cost can be reduced by up to 15%. The wingtip vortex suppression caused by the inboard-up rotating propeller can increase the maximum lift-drag ratio of the wing by 5.43%-6.65%; Increasing the number of rotors while reducing their diameter effectively improves the slipstream generation efficiency of the DEP, but reduces its overall thrust efficiency and increases its total noise. To maximize the overall efficiency, it is necessary to strike a balance between the DEP slipstream generation efficiency and DEP overall thrust efficiency when optimizing the tilt-wing cargo aircraft.

The proposed method fully considers the influence of the above factors at the initial design stage, and thus can be used to obtain a reasonable and balanced optimization design result with acceptable calculation cost, which provides a benchmark for the further design and analysis at the next design stage. This work provides a reference for the future optimization and design of the unmanned tilt-wing cargo aircraft with distributed propulsors.

REFERENCES

[1] M. H. Jones, S. D. Patek, and B. E. Tawney, "Unmanned aerial vehicle (UAV) cargo system," in *Proc. Syst. Inf. Eng. Des. Symp.*, vol. 2002, 2004, pp. 55–64.

[2] T. Crabtree, T. Huang, R. Tom, and G. Gildemann, "World air cargo forecast 2018-2037," Boeing, Chicago, IL, USA, Tech. Rep., 2018. [Online]. Available: https://www.boeing.com/commercial/market/cargo-forecast/

[3] D. Bamburry, "Drones: Designed for product delivery," *Des. Manage. Rev.*, vol. 26, no. 1, pp. 40–48, Jul. 2015.

[4] D. Floreano and R. J. Wood, "Science, technology and the future of small autonomous drones," *Nature*, vol. 521, no. 7553, pp. 460–466, May 2015.

[5] I. Gál, D. Rohács, and J. Rohács, "Developing the unmanned unconventional cargo airplanes with hybrid propulsion system," in *Proc. 31st Int. Council Aeronaut. Sci. (ICAS)*, 2018, pp. 1–10.

[6] A. S. Saeed, A. B. Younes, S. Islam, J. Dias, L. Seneviratne, and G. Cai, "A review on the platform design, dynamic modeling and control of hybrid UAVs," in *Proc. Int. Conf. Unmanned Aircr. Syst. (ICUAS)*, Jun. 2015, pp. 806–815.

[7] J. Keith and D. Hall, "Rapid sizing methodologies for VTOL UAVs," in *Proc. 47th AIAA Aerosp. Sci. Meeting Including New Horizons Forum Aerosp. Expo.*, Jan. 2009, pp. 1–11.

[8] U. Ozdemir, Y. O. Aktas, A. Vuruskan, Y. Dereli, A. F. Tarhan, K. Demirbag, A. Erdem, G. D. Kalaycioglu, I. Ozkol, and G. Inalhan, "Design of a commercial hybrid VTOL UAV system," *J. Intell. Robotic Syst.*, vol. 74, nos. 1–2, pp. 371–393, Apr. 2014.

[9] Y. O. Aktas, U. Ozdemir, Y. Dereli, A. F. Tarhan, A. Cetin, A. Vuruskan, B. Yuksek, H. Cengiz, S. Basdemir, M. Ucar, M. Genctav, A. Yukselen, I. Ozkol, M. O. Kaya, and G. Inalhan, "A low cost prototyping approach for design analysis and flight testing of the TURAC VTOL UAV," in *Proc. Int. Conf. Unmanned Aircr. Syst. (ICUAS)*, May 2014, pp. 1029–1039.

[10] J. Holsten, T. Ostermann, and D. Moormann, "Design and wind tunnel tests of a tiltwing UAV," *CEAS Aeronaut. J.*, vol. 2, nos. 1–4, pp. 69–79, Dec. 2011.

[11] A. R. Serrano, "Design methodology for hybrid (VTOL + fixed Wing) unmanned aerial vehicles," *Aeronaut. Aerosp. Open Access J.*, vol. 2, no. 3, Jun. 2018.

[12] S. S. Chauhan and J. R. Martins, "Tilt-wing eVTOL takeoff trajectory optimization," *J. Aircr.*, vol. 2019, no. 1, pp. 93–112, 2019.

[13] S. W. Ferguson, "A mathematical model for real time flight simulation of a generic tilt-rotor aircraft," Syst. Technol. Inc., Hawthorne, CA, USA, Tech. Rep. NACA-TR-1195-2, Sep. 1988.

[14] S. A. Ning, "A simple solution method for the blade element momentum equations with guaranteed convergence," *Wind Energy*, vol. 17, no. 9, pp. 1327–1345, 2014.

[15] M. L. Masquelier, "Application of the vortex-lattice method to propeller performance analysis," M.S. thesis, AFIT, Wright-Patterson AFB, OH, USA, 1982.

[16] M. A. Potsdam and R. C. Strawn, "CFD simulations of tiltrotor configurations in hover," *J. Amer. Helicopter Soc.*, vol. 50, no. 1, pp. 82–94, Jan. 2005.

[17] G. Klemstein and C. H. Liu, "Application of airfoil theory for nonuniform streams to wing propeller interaction," *J. Aircr.*, vol. 9, no. 2, pp. 137–142, Feb. 1972.

[18] J. T. Hwang and A. Ning, "Large-scale multidisciplinary optimization of an electric aircraft for on-demand mobility," in *Proc. AIAA/ASCE/AHS/ASC Struct., Struct. Dyn., Mater. Conf.*, Jan. 2018, vol. 2018, no. 210049, pp. 1–18.

[19] P. Lotstedt, "Accuracy of a propeller model in inviscid flow," *J. Aircr.*, vol. 32, no. 6, pp. 1312–1321, Nov. 1995.

[20] H.-Y. Xu, Z.-Y. Ye, and A.-M. Shi, "Numerical study of propeller slipstream based on unstructured dynamic overset grids," *J. Aircr.*, vol. 49, no. 2, pp. 384–389, Mar. 2012.

[21] S. Hong, J. Jeong, S. Kim, J. Suk, and J. I. Jung, "Longitudinal flight dynamics of a single tilt-wing unmanned aerial vehicle," *IFAC Proc. Volumes*, vol. 46, no. 19, pp. 60–65, 2013.
[22] Y. Wang, Y. Zhou, and C. Lin, "Modeling and control for the mode transition of a novel tilt-wing UAV," *Aerosp. Sci. Technol.*, vol. 91, pp. 593–606, Aug. 2019.
[23] K. Benkhoud and S. Bouallegue, "Model predictive control design for a convertible quad tilt-wing UAV," in *Proc. 4th Int. Conf. Control Eng. Inf. Technol. (CEIT)*, Dec. 2016, pp. 1–6.
[24] C. Hancer, K. T. Oner, E. Sirimoglu, E. Cetinsoy, and M. Unel, "Robust hovering control of a quad tilt-wing UAV," in *Proc. IECON-36th Annu. Conf. IEEE Ind. Electron. Soc.*, Nov. 2010, pp. 1615–1620.
[25] D. R. Mix, J. S. Koenig, K. M. Linda, O. Cifdaloz, V. L. Wells, and A. A. Rodriguez, "Towards gain-scheduled H^{∞} control design for a tilt-wing aircraft," in *Proc. 43rd IEEE Conf. Decis. Control (CDC)*, vol. 2, Dec. 2004, pp. 1222–1227.
[26] X. Wang and L. Cai, "Mathematical modeling and control of a tilt-rotor aircraft," *Aerosp. Sci. Technol.*, vol. 47, pp. 473–492, Dec. 2015.
[27] Y. Aoki and K. Muraoka, "Forward wing tip design for induced drag reduction of quad tilt wing VTOL un-manned plane in cruise," in *Proc. AIAA Scitech Forum*, Jan. 2019, p. 1307.
[28] P. Beaumier, J. Decours, and T. Lefebvre, "Aerodynamic and aero-acoustic design of modern tilt-rotors: The ONERA experience," in *Proc. ICAS-26th Congr. Int. Council Aeronaut. Sci.*, vol. 4, 2008, pp. 1669–1679.
[29] W. Jones, E. J. Nielsen, E. M. Lee-Rausch, and C. W. Acree, "Multi-point adjoint-based design of tilt-rotors in a noninertial reference frame," in *Proc. 10th AIAA Multidisciplinary Design Optim. Conf.*, Jan. 2014, pp. 1–18.
[30] A. Massaro and A. D'Andrea, "Multi-point aerodynamic optimization of advanced tiltrotor blades by means of memetic algorithms," in *Proc. 39th Eur. Rotorcr. Forum*, 2013, pp. 64–68.
[31] J. Lim, T. Kim, S. J. Shin, and D. H. Kim, "Structural integrity design of a composite wing in a tiltrotor aircraft," in *Proc. ICCM Int. Conf. Compos. Mater.*, 2011, pp. 1–5.
[32] J. Paik and F. Gandhi, "Design optimization for improved soft in-plane tiltrotor aeroelastic in airplane mode," *J. Aircr.*, vol. 47, no. 4, pp. 1089–1099, Jul. 2010.
[33] A. Radhakrishnan and F. Schmitz, "Quad tilt rotor aerodynamics in ground effect," in *Proc. 23rd AIAA Appl. Aerodynamics Conf.*, vol. 2, Jun. 2005, pp. 1290–1300.
[34] M. D. Moore and K. H. Goodrich, "High speed mobility through on-demand aviation," in *Proc. Aviation Technol., Integr., Oper. Conf.*, Aug. 2013, pp. 1–27.
[35] N. K. Borer, M. D. Moore, and A. Turnbull, "Tradespace exploration of distributed propulsors for advanced on-demand mobility concepts," in *Proc. 14th AIAA Aviation Technol., Integr., Oper. Conf.*, Jun. 2014, pp. 1–14.
[36] W. J. Fredericks, R. G. McSwain, B. F. Beaton, D. W. Klassman, and C. R. Theodore, "Greased lightning (GL-10) flight testing campaign," LaRC, Hampton, VA, USA, Tech. Rep. NASA/TM-2017-219643, Jul. 2017.
[37] G. Droandi, M. Syal, and G. Bower, "Tiltwing multi-rotor aerodynamic modeling in hover, transition and cruise flight conditions," presented at the AHS Int. 74th Annu. Forum Tech. Disp., Phoenix, AZ, USA, May 2018.
[38] Y. Pan, J. Huang, F. Li, and C. Yan, "Aerodynamic robust optimization of flying wing aircraft based on interval method," *Aircr. Eng. Aerosp. Technol.*, vol. 89, no. 3, pp. 491–497, May 2017.
[39] M. Konar, A. Turkmen, and T. Oktay, "Improvement of the thrust-torque ratio of an unmanned helicopter by using the ABC algorithm," *Aircr. Eng. Aerosp. Technol.*, to be published, doi: 10.1108/AEAT-03-2020-0057.
[40] X. Zhu, Z. Guo, Z. Hou, X. Gao, and J. Zhang, "Parameter's sensitivity analysis and design optimization of solar-powered airplanes," *Aircr. Eng. Aerosp. Technol.*, vol. 88, no. 4, pp. 550–560, Jul. 2016.
[41] M. Konar, "Simultaneous determination of maximum acceleration and endurance of morphing UAV with ABC algorithm-based model," *Aircr. Eng. Aerosp. Technol.*, vol. 92, no. 4, pp. 579–586, Mar. 2020.
[42] T. Oktay, S. Arik, I. Turkmen, M. Uzun, and H. Celik, "Neural network based redesign of morphing UAV for simultaneous improvement of roll stability and maximum lift/drag ratio," *Aircr. Eng. Aerosp. Technol.*, vol. 90, no. 8, pp. 1203–1212, Nov. 2018.
[43] F. Shahmiri, M. Sargolzehi, and M. A. S. Ashtiani, "Systematic evaluation of the helicopter rotor blades: Design variables and interactions," *Aircr. Eng. Aerosp. Technol.*, vol. 91, no. 9, pp. 1223–1237, Oct. 2019.
[44] B. S. de Mattos, P. J. Komatsu, and J. T. Tomita, "Optimal wingtip device design for transport airplane," *Aircr. Eng. Aerosp. Technol.*, vol. 90, no. 5, pp. 743–763, Jul. 2018.
[45] H. Soojung, K. Yushin, M. K. Lee, and M. K. Jai, "Tilt rotor/wing concept for multi-purpose VTOL UAV," in *Proc. Nat. Aerosp. Lab. NLR-32nd Eur. Rotorcr. Forum, ERF*, vol. 3, 2007, pp. 1537–1544.
[46] W. Tang and B.-F. Song, "Transitional flight equilibrium and performance study for the X-NMRL tail-sitter VTOL MAV," *Proc. Inst. Mech. Eng., G, J. Aerosp. Eng.*, vol. 233, no. 8, pp. 3056–3077, Jun. 2019.
[47] D. A. Spera, "Models of lift and drag coefficients of stalled and unstalled airfoils in wind turbines and wind tunnels," GRC, Cleveland, OH, USA, Tech. Rep. NASA/CR-2008-215434, Oct. 2008.
[48] E. N. Jacobs and R. F. Anderson, "Large-scale aerodynamic characteristics of airfoils as tested in the variable density wind tunnel," LAL, Langley Field, VA, USA, Tech. Rep. NACA-TR-352, 1931.
[49] M. Elgammi and T. Sant, "A new stall delay algorithm for predicting the aerodynamics loads on wind turbine blades for axial and yawed conditions," *Wind Energy*, vol. 20, no. 9, pp. 1645–1663, Sep. 2017.
[50] H. Amini and S. Steen, "Experimental and theoretical analysis of propeller shaft loads in oblique inflow," *J. Ship Res.*, vol. 55, no. 4, pp. 268–288, Dec. 2011.
[51] J.-H. He, "Improvement of Newton iteration method," *Int. J. Nonlinear Sci. Numer. Simul.*, vol. 1, no. 3, pp. 239–240, Jan. 2000.
[52] H. C. McLemore and M. D. Cannon, "Aerodynamic Investigation of a four-blade propeller operating through an angle of attack range from 0 to 180 degrees," LAL, Langley Field, VA, USA, Tech. Note NACA-TN-3228, Jun. 1954.
[53] O. . Gabor, A. Koreanschi, and R. M. Botez, "A new non-linear vortex lattice method: Applications to wing aerodynamic optimizations," *Chin. J. Aeronaut.*, vol. 29, no. 5, pp. 1178–1195, Oct. 2016.
[54] W. C. Schneider, "A comparison of the spanwise loading calculated by various methods with experimental loadings obtained on a 45° sweptback wing of aspect ratio 8.02 at a Reynolds number of 4.0×106," LAL, Langley Field, VA, USA, Tech. Rep. NACA-TN-1208, Aug. 1951.
[55] L. Veldhuis, "Propeller wing aerodynamic interference," Ph.D. dissertation, Fac. Aerosp. Eng. TU Delft, Delft, The Netherlands, 2005.
[56] E. P. Hartman and D. Biermann, "The aerodynamic characteristics of full-scale propellers having 2, 3 and 4 blades of clark Y and R.A.F 6 airfoil sections," LAL, Langley Field, VA, USA, Tech. Rep. NACA-TR-640, Jan. 1938.
[57] T. Sinnige, N. van Arnhem, T. C. A. Stokkermans, G. Eitelberg, and L. L. M. Veldhuis, "Wingtip-mounted propellers: Aerodynamic analysis of interaction effects and comparison with conventional layout," *J. Aircr.*, vol. 56, no. 1, pp. 295–312, Jan. 2019.
[58] E. B. Tingey and A. Ning, "Trading off sound pressure level and average power production for wind farm layout optimization," *Renew. Energy*, vol. 114, pp. 547–555, Dec. 2017.
[59] T. F. Brooks and M. A. Marcolini, "Airfoil tip vortex formation noise," *AIAA J.*, vol. 24, no. 2, pp. 246–252, Feb. 1986.
[60] J. Gundlach, *Designing Unmanned Aircraft Systems: A Comprehensive Approach*, 2nd ed. Washington, DC, USA: AIAA, 2014.
[61] M. D. Ardema, M. C. Chambers, A. P. Patron, A. S. Hahn, H. Miura, and M. D. Moore, "Estimation of transport aircraft analytical fuselage and wing weight," NASA, Washington, DC, USA, Tech. Memo. 110392, May 1996.
[62] E. Torenbeek, "Development and application of a comprehensive, design-sensitive weight prediction method for wing structures of transport category aircraft," Dept. Aerosp. Eng., TU Delft, Delft, The Netherlands, Tech. Rep. LR-693, 1992.
[63] J. Roskam, *Airplane Aerodynamics and Performance*. Lawrence, KS, USA: DARcorporation, 2003, p. 711.
[64] A. Silverstein, "Wind tunnel interference with particular reference to off center positions of the wing and to the downwash at the tail," LAL, Langley Field, VA, USA, Tech. Rep. NACA-TR-547, Jun. 1935.
[65] O. Gur, W. H. Mason, and J. A. Schetz, "Full-configuration drag estimation," *J. Aircr.*, vol. 47, no. 4, pp. 1356–1367, Jul. 2010.
[66] A. Dillmann and C. Wagner, *New Results in Numerical and Experimental Fluid Mechanics VI*. Berlin, German: Springer, 2008.
[67] A. Florian, "An efficient sampling scheme: Updated latin hypercube sampling," *Probabilistic Eng. Mech.*, vol. 7, no. 2, pp. 123–130, Jan. 1992.
[68] T. Murata and H. Ishibuchi, "MOGA: Multi-objective genetic algorithms," in *Proc. IEEE Int. Conf. Evol. Comput.*, Nov. 1995, pp. 289–294.

GANG CHEN received the B.S. degree in aircraft design from Beihang University, Beijing, China, in 2015, where he is currently pursuing the Ph.D. degree with the School of Aeronautic Science and Engineering. His current research interests include new concept aircraft design and optimization, hybrid-electric powertrain design, eVTOL aircraft design, and so on.

DONGLI MA received the B.S. and M.S. degrees in flight mechanics from Beihang University, Beijing, China, in 1990, and the Ph.D. degree in aircraft design from Beihang University, in 1996. Since 2001, he has been a Professor with Beihang University. His main research interests are aircraft design and UAV technology.

YUHONG JIA received the M.S. degree in mechanics and the Ph.D. degree in aircraft design from Beihang University, Beijing, China, in 1993 and 1999, respectively. She is currently a Professor with Beihang University. Her current research interests include aircraft design and aircraft structure design.

XINGLU XIA received the B.S. degree in aircraft design from Beihang University, Beijing, China, in 2016, where he is currently pursuing the Ph.D. degree with the School of Aeronautic Science and Engineering. His current research interests include new concept aircraft design, eVTOL aircraft design, and so on.

CHENG HE received the B.S. and M.S. degrees in aircraft design from Beihang University, Beijing, China, in 2018, where he is currently pursuing the Ph.D. degree with the School of Aeronautic Science and Engineering. His current research interests include aircraft design and aerodynamic design.